Wingbeat Time and the Scaling of Passive Rotational Damping in Flapping Flight

Tyson L. Hedrick,[1]* Bo Cheng,[2] Xinyan Deng[2]*

Flying animals exhibit remarkable capabilities for both generating maneuvers and stabilizing their course and orientation after perturbation. Here we show that flapping fliers ranging in size from fruit flies to large birds benefit from substantial damping of angular velocity through a passive mechanism termed flapping counter-torque (FCT). Our FCT model predicts that isometrically scaled animals experience similar damping on a per-wingbeat time scale, resulting in similar turning dynamics in wingbeat time regardless of body size. The model also shows how animals may simultaneously specialize in both maneuverability and stability (at the cost of efficiency) and provides a framework for linking morphology, wing kinematics, maneuverability, and flight dynamics across a wide range of flying animals spanning insects, bats, and birds.

Flying animals of all sizes exhibit a surprising degree of maneuverability, and animals ranging in size from fruit flies (1) to pigeons (2) have been the subject of detailed analyses of maneuvering kinematics. Many studies have also considered stability and control in animal flight, both from a neural standpoint (3, 4) and in broader analyses incorporating both neural and physical inputs (5–7). This body of work provides the opportunity to examine the scaling of maneuvering capability with body size and determine whether animals of different sizes and phylogenetic groups use similar or different mechanisms to accomplish maneuvers.

We focus our comparison on a particular type of maneuver: low-speed yaw turns of 60° or more (Fig. 1), because these have been most widely recorded in freely flying animals. Rotational maneuvers such as yaw turns necessarily include both an angular acceleration phase, where the animal begins turning, and an angular deceleration phase, where the animal slows and ends the rotation. In the acceleration phase, the animal must actively produce an aerodynamic torque through some type of flapping or body asymmetry. However, the animal might then decelerate by either actively producing a torque in the opposite direction (1) or simply allowing friction to passively damp out its rotational velocity, coasting to a halt. Because the moment of inertia is proportional to mass to the five-thirds power (mass$^{5/3}$), large animals such as birds are likely to require active deceleration whereas smaller animals such as flies are often modeled with substantial fluid drag (8), which might allow passive deceleration, although a recent report emphasizes active deceleration in these animals as well (1). However, other recent analyses of yaw turns in insects (9) and banked turns in birds (10) emphasized the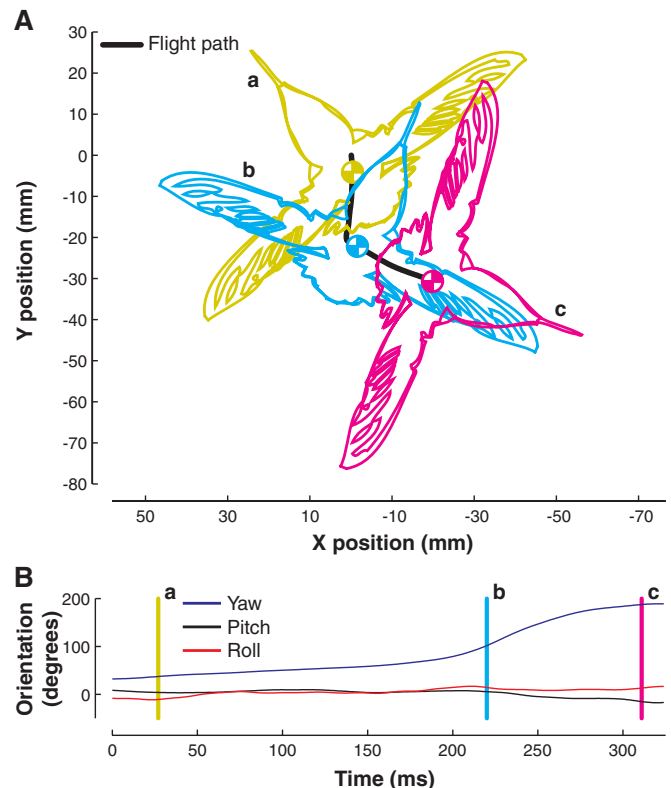 importance of a form of aero-dynamic damping related to symmetric wing motion, raising the possibility that passive damping is important at many size scales.

Damping from wing motion arises as follows: Consider an animal engaged in symmetric hovering or low-speed flight (Fig. 2, A and B). Previous experiments have shown that during downstroke, net aerodynamic forces are directed upward and posteriorly; in upstroke, in animals with an aerodynamically active upstroke, the forces are directed upward and anteriorly (11, 12). However, when the animal experiences whole-body rotation (for example, about an axis normal to the plane of flapping), net wing velocity is enhanced on the outside wing during downstroke and on the inside wing during upstroke (2). This net velocity asymmetry, which arises when the animal is flapping symmetrically, gives rise to a force asymmetry (and therefore a torque) that acts to slow the animal's rotation (Fig. 2, C and D). We refer to this form of damping as FCT because it depends on flapping and acts counter to the direction of body rotation. Below, we explore the scaling implications of FCT by postulating a simple equation modeling FCT and a second equation modeling active torque generation via asymmetric flapping, the expected deceleration method for large animals because of the rapid increase in moment of inertia with body size. We use these two equations to develop alternative predictions of the rotational deceleration dynamics for flying animals and then compare the predictions to measurements of yaw turning in four species of insects and three species of vertebrates across six orders of magnitude in body mass (from 1×10^{-4} to 285 g). The results of the comparison are consistent with FCT but not with an active deceleration via asymmetric flapping.

The rotational damping due to FCT arises from the difference in velocity between the inside and outside wings (Fig. 2, C and D). Thus, FCT is the result of (velocity due to flapping – velocity due to body rotation)^2 on one wing minus (velocity due to flapping + velocity due to rotation)^2 on the other wing, multiplied by the determinants of aerodynamic force: air density; wing size and shape; and where flapping velocity is determined by amplitude, frequency, and trajectory. Angular deceleration resulting from FCT is therefore

[1]Department of Biology, University of North Carolina at Chapel Hill, Chapel Hill, NC 27599, USA. [2]Department of Mechanical Engineering, University of Delaware, Newark, DE 19716, USA.

*To whom correspondence should be addressed. E-mail: thedrick@bio.unc.edu (T.L.H.); deng@udel.edu (X.D.)

Fig. 1. A sharp yaw turn performed by a hovering ruby-throated hummingbird. (**A**) The hummingbird's position and orientation in the horizontal (x-y) plane at three different times during the turn, viewed from above the bird, looking down. The +z axis points into the page and toward the ground, parallel to gravity. The hummingbird yaws to its right, corresponding to a clockwise motion on the figure between stages a, b, and c. The hummingbird is to scale, but the wing position in the figure does not indicate the actual wing position. In addition to the horizontal movement depicted here, the hummingbird descended 25 mm during the recording. (**B**) The hummingbird's yaw, pitch, and roll orientation through time. The vertical lines a, b, and c indicate the time represented by each of the outline figures in (A).

proportional to angular velocity and inversely proportional to the animal's moment of inertia. These factors may be expressed concisely by the following ordinary differential equation

$$\dot{\omega}_{FCT} = -\omega \frac{\rho R^4 \overline{c}\, \hat{r}_3^3(S)\Phi n \overline{C_F \sin(\alpha)(d\hat{\varphi}/d\hat{t})}}{I} \tag{1}$$

where $\dot{\omega}_{FCT}$ is angular deceleration due to FCT, ω is angular velocity, $\overline{C}_F$ is the mean aerodynamic resultant force coefficient, α is the spanwise rotation angle of the wing, ρ is air density, R is wing length, $\overline{c}$ is the average wing chord, $\hat{r}_3(S)$ is the nondimensional third moment of area, Φ is wing stroke amplitude, n is wingbeat frequency, $(d\hat{\varphi}/d\hat{t})$ is the nondimensional wing angular velocity, and I is the animal's moment of inertia. All symbols are as per Ellington (13). See appendix A in (14) for background on this equation.

An alternative to deceleration by FCT, active torque generation by asymmetric flapping, depends on the degree of functional asymmetry between the two wings; deceleration due to asymmetric flapping may be written as

$$\dot{\omega}_a = (\gamma - 1)\frac{\rho R^4 \overline{c}\, \hat{r}_3^3(S)\Phi^2 n^2 \overline{C_F \sin(\alpha)(d\hat{\varphi}/d\hat{t})^2}}{8I} \tag{2}$$

where γ is the magnitude of the asymmetry, ranging from 0 to 1, with 1 indicating no asymmetry. Unlike FCT, active deceleration is not related to body angular velocity. See appendix B in (14) for additional details on this formulation.

It is known that the dimensions of flying animals scale at near isometry, with wing length and chord proportional to mass$^{1/3}$ and moment of inertia proportional to mass$^{5/3}$ (15). Wingbeat frequency is known to scale as mass$^{-0.24}$ for insects and hummingbirds, but the fit is poor and there is substantial variation within a given size range (16). Therefore, after assuming isometric scaling and eliminating nonvarying and nondimensional terms from Eqs. 1 and 2, we are left with the following proportionalities

$$\dot{\omega}_{FCT} \propto -\omega\Phi n \tag{3}$$

$$\dot{\omega}_a \propto (\gamma - 1)\Phi^2 n^2 \tag{4}$$

Fig. 2. FCT arises when overall body rotation interacts with symmetric wing motion. (**A**) and (**B**) show the aerodynamic forces experienced by a flying animal in upstroke (A) and downstroke (B). (**C**) and (**D**) show how wing motion and aerodynamic forces are modified by overall body rotation. The now asymmetric aerodynamic forces provide a torque counter to the body rotation.

— Net wing motion — Aerodynamic force vectors
···· Body rotation ⊕ Center of mass
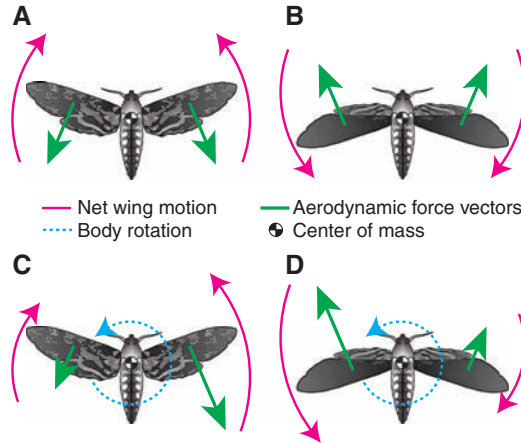
Table 1. Morphological data and predictions from the active and passive deceleration hypotheses along with the measurements. I'_{zz}, moment of inertia of the animal in the stroke plane frame yaw axis; $t_{1/2}(N)$, half-life as a function of number of wingbeats. See (14) for details of the FCT and active deceleration predictions as well as the sources of the morphological and kinematic data. Active deceleration predictions are for the time required to decelerate to one-half of peak velocity, making them directly comparable to the FCT predictions. We used a γ of 0.944, based on an arithmetic solution of Eq. 2 to the fruit fly data. See (14) for results scaling γ to body size or other factors. For both sets of predictions, we assume that $\overline{C_F \sin(\alpha)(d\hat{\varphi}/d\hat{t})}$ is equal to 6.0 and $\overline{C_F \sin(\alpha)(d\hat{\varphi}/d\hat{t})^2}$ is equal to 31.3 for all species.

Species	Morphology							FCT passive deceleration predictions		Active deceleration predictions		Measurements	
	Mass (g)	I'_{zz} (N·m s²)	R (mm)	$\overline{c}$ (mm)	n (Hz)	Φ (°)	$\hat{r}_3(S)$ (—)	$t_{1/2}(t)$ (ms)	$t_{1/2}(N)$ (wingbeats)	$t_{1/2}(t)$ (ms)	$t_{1/2}(N)$ (wingbeats)	$t_{1/2}(t)$ (ms)	$t_{1/2}(N)$ (wingbeats)
Fruit fly (*Drosophila melanogaster*)	$9.6 \pm 2.7 \times 10^{-4}$	2.72×10^{-13} —	2.39 ± 0.08	0.80 ± 0.02	218 ± 7	140 ± 10	0.59	9.2 ± 1.5	2.00 ± 0.32	10.4 ± 2.3	2.22 ± 0.48	10.36	2.2
Stalk-eyed fly (*Cyrtodiopsis dalmanni*)	$7.0 \pm 1.0 \times 10^{-3}$	1.60×10^{-11} —	4.46 ± 0.14	0.94 ± 0.08	170 ± 8	$140* \pm 10$	0.64	38.0 ± 11.1	6.47 ± 1.85	55.1 ± 11.8	9.35 ± 1.82	35.68	5.6
Bluebottle fly (*Calliphora vicina*)	$6.2 \times 10^{-2} \pm 5.0 \times 10^{-3}$	2.81×10^{-10} —	9.2 ± 0.5	3.14 ± 0.5	143 ± 9	138 ± 15	0.59	17.2 ± 11.7	2.43 ± 1.63	30.8 ± 15.0	4.32 ± 2.01	14.31	2.1
Hawkmoth (*Manduca sexta*)	1.62 ± 0.33	2.43×10^{-7} —	48.8 ± 2.1	18.6 ± 1.6	26 ± 2	98 ± 4	0.56	28.4 ± 6.6	0.74 ± 0.16	166.1 ± 46.3	4.31 ± 1.02	19	0.5†
Hummingbird (*Archilochus colubris*)	3.17 ± 0.15	3.58×10^{-7} —	45.0 ± 4.7	11.8 ± 2.0	48.7 ± 9.1	134 ± 7.2	0.57	33.8 ± 26.1	1.64 ± 1.13	184.1 ± 180.2	8.86 ± 6.12	45	2.0†
Fruit bat (*Cynopterus brachyotis*)	35.1 ± 1.8	4.12×10^{-5} —	150 ± 14	83 ± 14	11.1 ± 0.6	141 ± 14	0.54	22.0 ± 12.3	0.24 ± 0.14	415.4 ± 256.5	4.60 ± 2.77	17	0.2†
Cockatoo (*Eolophus roseicapillus*)	285.9 ± 14.4	1.29×10^{-3} —	347 ± 8	118 ± 4	7.1 ± 1.1	99 ± 16.4	0.58	30.3 ± 6.4	0.22 ± 0.02	945.4 ± 392.5	6.72 ± 1.37	40	0.3†

*A wingbeat amplitude measure was not available for the stalk-eyed fly; *Drosophila* kinematics were substituted. †The measurement of half-life in wingbeats uses the animal's exact wingbeat frequency when available.

where $\dot{\omega}$ is body angular deceleration due to FCT or active (a) means, ω is body angular velocity, Φ is wingbeat amplitude, n is wingbeat frequency, and γ is the magnitude of asymmetry in flapping. Wingbeat amplitude is not known to vary widely or systematically among species, whereas wingbeat frequency varies over two orders of magnitude (15) and from 218 to 7.1 Hz in the species examined here. Thus, variation in these equations among different species is dominated by variation in wingbeat frequency.

These equations summarize two distinct modes by which flying animals might reduce their angular velocity at the end of a maneuver. Yaw deceleration dominated by FCT would exhibit exponential decay (Eqs. 1 and 3 and eqs. S19 to S23), a pattern observed in early studies of fruit fly turning (17, 18) and ascribed to body friction. For animals of approximately isometric dimensional scaling, similar wingbeat amplitudes, and similar aerodynamic force coefficients, Eq. 3 also implies that normalizing time by wingbeat frequency should result in similar wingbeat time dynamics regardless of body size (eq. S23). Deceleration due to the simple model of asymmetric flapping (Eqs. 2 and 4) is linear and occurs at a rate that varies with the square of flapping frequency.

We tested predictions of turning dynamics arising from these two modes against data from seven different animals executing low-speed yaw turns (Fig. 1 and Table 1). See appendix C in (14) for a description of the various sources of these data, both in the literature and from previously unreported experiments.

Unsurprisingly, given the considerable range of species examined, the different animals exhibited widely divergent yaw turning performance (Fig. 3A and Table 1), slowing down at very different rates. However, in contrast to their differences in deceleration rate, the fruit fly, stalk-eyed fly, bluebottle fly, and hummingbird all exhibited similar peak yaw rates of approximately 1600° s^{-1}. This does not appear to reflect a mechanical limitation, because Eq. 2 indicates that these animals should have greatly different capabilities for active torque generation and even different ratios of active torque to FCT (Eq. 5). It may reflect neurophysiological limitations on the rate at which flying animals can acquire and process sensory information for flight control (19).

The measured duration of yaw rate half-life during deceleration was similar to that predicted by the FCT passive deceleration model (Eq. 1, Table 1, and Fig. 3D). The deceleration rate, measured as the time to decelerate to one-half the peak yaw rate, was not similar to that predicted for active torque generation (Eq. 2 and Table 1). Furthermore, the prediction that approximately isometric animals should have similar rotational deceleration dynamics in wingbeat time was also supported (Fig. 2B). This prediction is specific to isometrically scaled animals; the data reveal two such groups with similar dynamics. Fruit flies,

bluebottle flies, and hummingbirds have similar scaling of wing and body dimensions (table S1) and all exhibited a deceleration half-life of about two wingbeats. Hawkmoths, bats, and cockatoos all have wings approximately twice as large relative to body weight as those of the aforementioned group and all exhibited half-lives of less than a wingbeat. The stalk-eyed fly has a moment of inertia out of proportion to body size due to its unusual eye position (20) and had a half-life of about six wingbeats.

Our FCT model predicts yaw turn deceleration dynamics across seven phylogenetically and morphologically dissimilar flying animals spanning six orders of magnitude in body mass (Fig. 3), using only morphological and kinematic inputs, supporting FCT as a unifying principle central to the dynamics of flying animals across a large size range. Our results do not agree with a model based on deceleration via torque generation by

asymmetric flapping. However, interspecific or temporal variation in asymmetry (γ) could produce the observed results—a perfectly valid although less parsimonious possibility. However, the appropriate variation in γ cannot be produced by scaling it from any of the measured morphological parameters [appendix D in (14) and fig. S3].

In addition to providing a framework for assessing animal flight dynamics, FCT also provides insights into form/function relationships. For example, maneuverability and stability are often cast in opposition to one another, but some factors that enhance maneuverability would also enhance FCT, a form of passive stability. The scaling of rotational maneuverability may be approximated by the same equation we use to estimate the scaling of deceleration via active torque generation (Eq. 2). Thus, increases in wingbeat frequency (n) in particular improve both an animal's aerodynamic capacity for torque generation
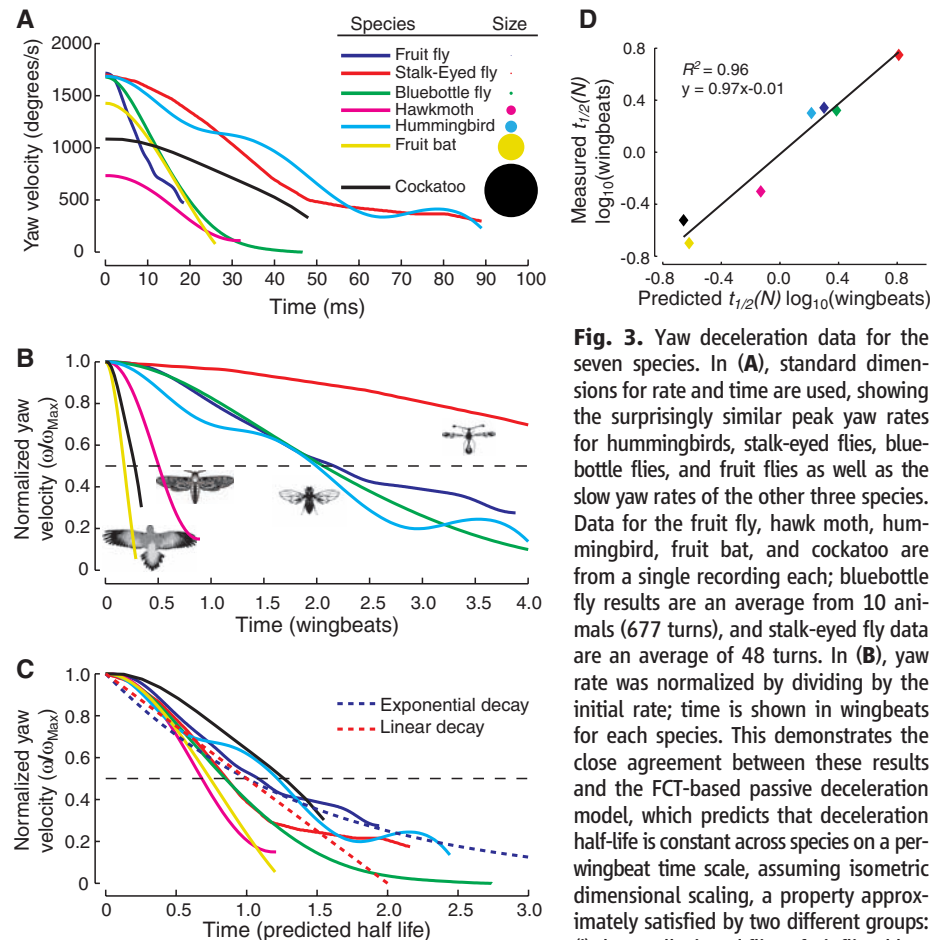
Fig. 3. Yaw deceleration data for the seven species. In (**A**), standard dimensions for rate and time are used, showing the surprisingly similar peak yaw rates for hummingbirds, stalk-eyed flies, bluebottle flies, and fruit flies as well as the slow yaw rates of the other three species. Data for the fruit fly, hawk moth, hummingbird, fruit bat, and cockatoo are from a single recording each; bluebottle fly results are an average from 10 animals (677 turns), and stalk-eyed fly data are an average of 48 turns. In (**B**), yaw rate was normalized by dividing by the initial rate; time is shown in wingbeats for each species. This demonstrates the close agreement between these results and the FCT-based passive deceleration model, which predicts that deceleration half-life is constant across species on a per-wingbeat time scale, assuming isometric dimensional scaling, a property approximately satisfied by two different groups: (i) the small-winged fliers: fruit flies, blue-bottle flies, and hummingbirds; and (ii) the large-winged fliers: hawk moths, bats, and cockatoos. See table S1 for a comparison of wing and body scaling among these species. In (**C**), yaw rate is normalized as in (**B**) and time is normalized to the predicted half-life of each species (Table 1). Ideal exponential decay (FCT) and linear decay (asymmetric flapping) curves are also shown. (**D**) compares the predicted and measured yaw deceleration half-life across the seven species. $t_{1/2}(N)$, half-life as a function of number of wingbeats. As expected, there was a strong relationship between predicted and measured values, and the least-squares regression slope is similar to 1.0 and the regression intercept close to 0, showing that the FCT model accurately predicts deceleration half-life for this group of species, despite the wide range of body sizes, differences in body and wing morphology, and phylogenetic distance.

and the magnitude of FCT. Because active torque is proportional to n^2 and passive torque to n, the ratio of active to passive torque increases as n increases (Eq. 5), even while both quantities increase individually

$$\frac{\dot{\omega}_{a}}{\dot{\omega}_{FCT}} = -(\gamma-1)\frac{\Phi n \,\overline{(d\hat{\varphi}/d\hat{t})}}{8\omega} \qquad (5)$$

The increase in the ratio indicates an enhanced capability for active maneuvers and active stabilization, whereas the increase in FCT adds to passive stability. Thus, increasing wingbeat frequency enhances both maneuverability and stability. Hummingbirds provide an interesting example; males typically have greater wingbeat frequencies (21) and smaller body sizes as compared to females of the same species, potentially conferring a benefit in maneuverability and therefore an advantage in display flights (22) as well as greater stability when experiencing an external perturbation. These benefits are not without cost, because increasing wingbeat frequency increases the inertial and profile power requirements of flapping flight.

Finally, the success of our FCT model in predicting yaw deceleration dynamics implies that passive damping may be important to flight control in flying animals across a wide range of body sizes. For example, if a steadily flapping animal experiences a brief perturbation in midstroke, by the time it is prepared to execute a corrective wingbeat, FCT will have eroded much of the effect of the perturbation, regardless of the wingbeat frequency employed by the animal. Thus, FCT provides open loop stability for some aspects of animal flight, reducing its neuromuscular and

neurosensory requirements. These are not eliminated, because FCT results in asymmetric forces from symmetric flapping, implying that the animal's muscles must generate asymmetric forces and suggesting neural regulation to enforce symmetry. Furthermore, FCT does not address all the stability problems faced by flying animals. This study is limited to yaw dynamics in hovering or slow-speed flight; FCT is likely to be influential in fast forward flight, but no data are available to test such predictions. More important, a full description of body dynamics involves many factors beyond FCT and includes modes such as pitching and longitudinal dynamics known to be inherently unstable in open loop conditions (23, 24) and subject to active control (25, 26). Finally, yaw damping due to FCT is a feature of flapping flight that is not found in human-made fixed-wing or rotary-wing flyers and may lead to improvements in the stability and maneuverability of biomimetic micro–air vehicles.

References and Notes

1. S. N. Fry, R. Sayaman, M. H. Dickinson, *Science* **300**, 495 (2003).
2. D. R. Warrick, K. P. Dial, *J. Exp. Biol.* **201**, 655 (1998).
3. M. F. Land, T. S. Collett, *J. Comp. Physiol. A* **89**, 331 (1974).
4. J. W. S. Pringle, in *Insect Flight*, M. Abercrombie, P. B. Medawar, G. Salt, M. M. Swann, V. B. Wigglesworth, Eds. (Cambridge Monographs in Experimental Biology, Cambridge Univ. Press, London, 1957), pp. 86–118.
5. G. K. Taylor *et al.*, *J. Exp. Biol.* **211**, 258 (2008).
6. G. K. Taylor, *Biol. Rev. Camb. Philos. Soc.* **76**, 449 (2001).
7. H. Wagner, *Philos. Trans. R. Soc. London Ser. B* **312**, 527 (1986).
8. N. Boeddeker, M. Egelhaaf, *J. Exp. Biol.* **208**, 1563 (2005).
9. T. Hesselberg, F.-O. Lehmann, *J. Exp. Biol.* **210**, 4319 (2007).
10. T. L. Hedrick, A. A. Biewener, *J. Exp. Biol.* **210**, 1897 (2007).
11. S. P. Sane, *J. Exp. Biol.* **206**, 4191 (2003).
12. J. R. Usherwood, C. P. Ellington, *J. Exp. Biol.* **205**, 1565 (2002).
13. C. P. Ellington, *Philos. Trans. R. Soc. London Ser. B* **305**, 41 (1984).
14. See supporting material on *Science* Online.
15. C. H. Greenewalt, *Smithson. Misc. Collect.* **144**, 1 (1962).
16. R. Dudley, *The Biomechanics of Insect Flight. Form, Function, Evolution* (Princeton Univ. Press, Princeton, NJ, 2000).
17. M. Mayer, K. Vogtmann, B. Bausenwein, R. Wolf, M. Heisenberg, *J. Comp. Physiol. A* **163**, 389 (1988).
18. H. H. Bülthoff, T. Poggio, C. Wehrhahn, *Z. Naturforsch. C* **35**, 811 (1980).
19. G. K. Taylor, H. G. Krapp, in *Insect Mechanics and Control*, J. Casas, S. J. Simpson, Eds. (Academic Press, London, 2007), vol. 34, pp. 231–316.
20. G. Ribak, J. Swallow, *J. Comp. Physiol. A* **193**, 1065 (2007).
21. T. A. Hunter, J. Picman, *Condor* **107**, 570 (2005).
22. F. G. Stiles, D. L. Altshuler, R. Dudley, *Auk* **122**, 872 (2005).
23. G. K. Taylor, A. L. R. Thomas, *J. Theor. Biol.* **214**, 351 (2002).
24. M. Sun, J. K. Wang, *J. Exp. Biol.* **210**, 2714 (2007).
25. G. K. Taylor, A. L. R. Thomas, *J. Exp. Biol.* **206**, 2803 (2003).
26. X. Deng, L. Schenato, S. S. Sastry, *IEEE Trans. Robotics* **22**, 789 (2006).
27. We thank A. Biewener of Harvard University and S. Swartz and K. Breuer of Brown University for providing the hummingbird and fruit bat data. This work was funded in part by NSF grant 0732267 (Division of Integrative Organismal Systems) to T.L.H. and NSF grant 0545931 (Division of Information and Intelligent Systems) to X.D.

Coding-Sequence Determinants of Gene Expression in *Escherichia coli*

Grzegorz Kudla,[1]* Andrew W. Murray,[2] David Tollervey,[3] Joshua B. Plotkin[1]†

Synonymous mutations do not alter the encoded protein, but they can influence gene expression. To investigate how, we engineered a synthetic library of 154 genes that varied randomly at synonymous sites, but all encoded the same green fluorescent protein (GFP). When expressed in *Escherichia coli*, GFP protein levels varied 250-fold across the library. GFP messenger RNA (mRNA) levels, mRNA degradation patterns, and bacterial growth rates also varied, but codon bias did not correlate with gene expression. Rather, the stability of mRNA folding near the ribosomal binding site explained more than half the variation in protein levels. In our analysis, mRNA folding and associated rates of translation initiation play a predominant role in shaping expression levels of individual genes, whereas codon bias influences global translation efficiency and cellular fitness.

The theory of codon bias posits that preferred codons correlate with the abundances of iso-accepting tRNAs (1, 2) and thereby increase translational efficiency (3) and accuracy (4). Recent experiments have revealed other effects of silent mutations (5–7). We synthesized a library of green fluorescent protein (GFP) genes that varied randomly in their codon usage, but encoded the same amino acid sequence (8). By placing these constructs in identical regulatory contexts and measuring their expression, we isolated the effects of synonymous variation on gene expression.

The GFP gene consists of 240 codons. For 226 of these codons, we introduced random silent mutations in the third base position, while keeping the first and second positions constant (Fig. 1A). The resulting synthetic GFP constructs differed by up to 180 silent substitutions, with an average of 114 substitutions between pairs of constructs (Fig. 1B and figs. S1 and S2). The range of third-position GC content (GC3) across the library of constructs encompassed virtually all (99%) of the GC3 values among endogenous *Escherichia coli* genes, and the variation in the codon adaptation index (CAI) (9) contained most (96%) of the CAI values of *E. coli* genes (Fig. 1).

We expressed the GFP genes in *E. coli* using a T7-promoter vector, and we quantified expression by spectrofluorometry. Fluorescence levels varied 250-fold across the library, and they were highly reproducible for each GFP construct (Spearman $r = 0.98$ between biological replicates) (fig. S3). Fluorescence variation was consistent across a broad range of experimental conditions (fig. S4).

[1]Department of Biology and Program in Applied Mathematics and Computational Science, The University of Pennsylvania, Philadelphia, PA 19104, USA. [2]Department of Molecular and Cellular Biology, Harvard University, Cambridge, MA 02138, USA. [3]Wellcome Trust Centre for Cell Biology and Centre for Systems Biology, University of Edinburgh, Edinburgh EH9 3JR, UK.

*Present address: Wellcome Trust Centre for Cell Biology, University of Edinburgh, Edinburgh EH9 3JR, UK.
†To whom correspondence should be addressed. E-mail: jplotkin@sas.upenn.edu

Supporting Online Material for

Wingbeat Time and the Scaling of Passive Rotational Damping in Flapping Flight

Tyson L. Hedrick,* Bo Cheng, Xinyan Deng*

*To whom correspondence should be addressed. E-mail: thedrick@bio.unc.edu (T.L.H.); deng@udel.edu
(X.D.)

This PDF file includes:

SOM Text
Figs. S1 to S3
Table S1
References
Appendices A to D

Supporting Online Material

List of Symbols

$\bar{c}$	Average wing chord
C_F	Coefficient of aerodynamic force
F	Force
I	Moment of inertia
$\mathbf{I}$	Moment of inertia matrix
$\mathbf{I}_b$	Moment of inertia matrix (body)
$\mathbf{I}_{wings}$	Moment of inertia matrix (wings)
I_{ZZ}	Moment of inertia in the body yaw axis
I'_{ZZ}	Moment of inertia of the animal in the stroke plane frame yaw axis
L	Torque about the X axis
M	Torque about the Y axis
n	Wingbeat frequency
N	Torque about the Z axis; Number of wingbeats
$\hat{r}_2(S)$	Non-dimensional second moment of wing area
$\hat{r}_3(S)$	Non-dimensional third moment of wing area
p	Roll velocity
q	Pitch velocity
r	Yaw velocity
R	Wing length
$t_{1/2}(N)$	Half life as a function of number of wingbeats
$t_{1/2}(t)$	Half life as a function of time
T	Torque
T_a	Torque due to aerodynamic forces
T_f	Torque due to friction
$\hat{t}$	Non-dimensional time
α	Wing spanwise rotation angle
θ	Wing angular position (deviation from stroke plane)
ϕ	Wing angular position (in the stroke plane)
$\hat{\phi}$	Non-dimensional wing angular position (in the stroke plane)
Φ	Wing stroke amplitude (in the stroke plane)
γ	Wing stroke asymmetry factor
ρ	Air density
ω	Angular velocity
$\dot{\omega}$	Angular acceleration
$\dot{\omega}_{FCT}$	Angular acceleration due to FCT
$\dot{\omega}_a$	Angular acceleration due to asymmetric flapping
Ω_b	Angular velocity of body in the stroke plane frame

Ω_w Angular velocity of the wing in the body frame

$\left(d\hat{\phi} / d\hat{t} \right)$ Non-dimensional wing angular velocity

·   Derivative with respect to time

Figure S1
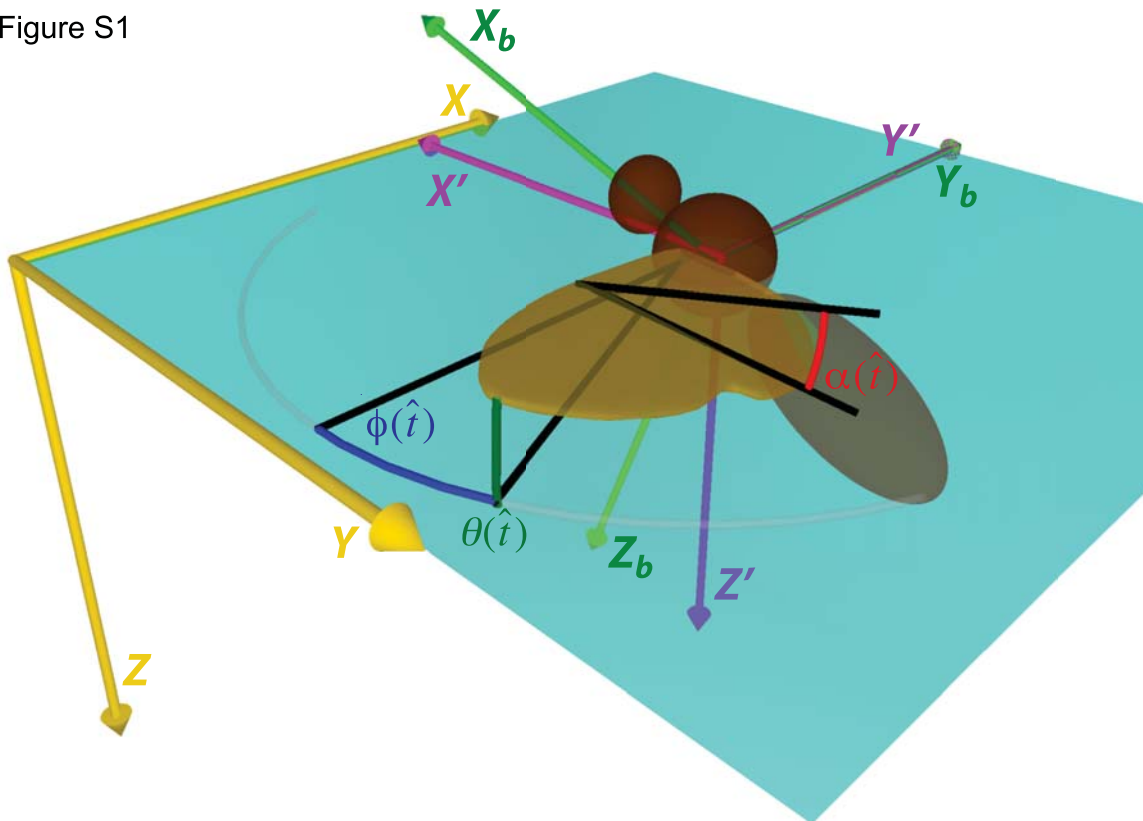
A sketch of an insect with one wing showing the global reference frame axes $X\,Y\,Z$, body reference frame axes $X_b\,Y_b\,Z_b$, wing stroke plane frame axes $X'\,Y'\,Z'$, wing stroke position angle ϕ, wing stroke deviation angle θ and wing spanwise rotation angle α. In the analysis presented here, the global and wing stroke plane frame Z axes are assumed to remain parallel throughout the turn, such that yaw in the wing stroke plane frame is also yaw in the global reference frame. Amplitude in θ was small compared to amplitude in ϕ over the course of the wingbeat cycle. The wing spanwise rotation angle α is zero when the wing surface is in the horiztonal plane; α was assumed to vary between 45 and -45 degrees.

Appendix A: Flapping counter-torque derivation

First consider the equations of motion for the angular dynamics in three dimensions of a flying animal:

$$\mathbf{I}_b \dot{\omega} + \omega \times \mathbf{I}_b \omega = T_a + T_f + T_L + T_R$$

(S1)

where T_L and T_R are torques (at the animal's center of mass) due to inertia of the left and right wing, and $\mathbf{I}_b$ is the body moment of inertia. Because the net inertial torque $T_L + T_R$ is small compared to aerodynamic torque during turning, we approximate the net inertial torque by adding the wing moments of inertia $\mathbf{I}_{wings}$ to the body moment of inertia $\mathbf{I}_b$ to get a total moment of inertia $\mathbf{I}$. Net inertial torque is small because for symmetric wing motion in hovering, net inertial torque has a half-wingbeat mean of zero in the pitch axis and an instantaneous mean of zero in the roll and yaw axes. Note that all variables are expressed with respect to the stroke plane coordinates (Fig. S1).

$$\mathbf{I} = \mathbf{I}_b + \mathbf{I}_{wings}$$

(S2)

and Eqn. S1 becomes:

$$\mathbf{I} \dot{\omega} + \omega \times \mathbf{I} \omega = T_a + T_f$$

(S3)

where $\mathbf{I}$ is the moment of inertia matrix:

$$\mathbf{I} = \begin{bmatrix} I'_{xx} & 0 & I'_{xz} \\ 0 & I'_{yy} & 0 \\ I'_{xz} & 0 & I'_{zz} \end{bmatrix}$$

(S4)

continuing the expansion of Eqn. S3, ω is body angular velocity and $\dot{\omega}$ its derivative, angular acceleration:

$$\omega = [p, q, r]^T$$

(S5)

T_a and T_f are torque due to aerodynamic forces and to body friction, respectively and *p, q, r* are the body angular velocities with respect to the wing frame axes (Fig. S1). Torque due to body friction has been shown to be negligible (S*1*) for animals as small as fruit flies. Larger

animals, with a smaller surface area to volume ratio, will be even less affected; T_f is not considered further. Aerodynamic torque may be written as:

$$T_a = [L, M, N]^T \qquad (S6)$$

where *L*, *M*, *N* are the torque in the roll, pitch and yaw axes. We then extract the term for yaw rotation from Eqn. S3 as:

$$I'_{zz}\dot{r} - I'_{xz}\dot{p} = (I'_{xx} - I'_{yy})pq - I'_{xz}qr + N \qquad (S7)$$

Terms $I'_{xz}\dot{p}$, $(I'_{xx} - I'_{yy})pq$ and $I'_{xz}qr$ are negligible due to the small roll (*p*) and pitch velocities (*q*) and accelerations exhibited by animals engaged in yaw turns (see Fig. 1 and fruit fly data in S1), leaving:

$$I'_{zz}\dot{r} = N \qquad (S8)$$

This equation, relating yaw acceleration to yaw moment of inertia and yaw torque, no longer includes any coupling terms between different axes of rotation and allows us to consider yaw angular dynamics independent of the other rotations. From this point forward, ω refers to scalar yaw angular velocity and *T* to yaw torque.

We now proceed with a standard blade-element model for aerodynamic force generation from a single flapping wing at a particular instant in the wing stroke cycle (S*2-4*), following the wing position and motion description in Figure S1:

$$F(\hat{t}) = \frac{C_F(\hat{t})\rho R^3 \bar{c}\,\hat{r}_2^2(S)\Phi^2 n^2 (d\hat{\phi}/d\hat{t})^2}{8} \qquad (S9)$$

where $C_F(\hat{t})$ is the mean aerodynamic resultant force coefficient at non-dimensional time $\hat{t}$, ρ is air density, *R* is wing length, $\bar{c}$ is the average wing chord, $\hat{r}_2^2(S)$ is the square of the non-dimensional second moment of area, Φ is wing stroke amplitude, *n* is wingbeat frequency, and $(d\hat{\phi}/d\hat{t})$ is the non-dimensional wing angular velocity.

We then convert this force to a torque in the stroke plane by introducing the moment arm of the center of pressure and assuming that aerodynamic force acts normal to the wing,

giving a horizontal projection of $\sin(\alpha)$, where α of zero indicates that the wing lies in the horizontal plane:

$$T(\hat{t}) = \frac{C_F(\hat{t})\sin(\alpha(\hat{t}))\rho R^4 \overline{c}\,\hat{r}_3^3(S)\Phi^2 n^2 \left(d\hat{\phi}/d\hat{t}\right)^2}{8} \tag{S10}$$

where $\alpha(\hat{t})$ is the wing's spanwise rotation angle and $\hat{r}_3^3(S)$ is the cube of the non-dimensional third moment of area.

We then separate equation S10, torque from a single wing, into non-kinematic and kinematic terms; C and Ω_w respectively:

$$C = \frac{C_F(\hat{t})\sin(\alpha(\hat{t}))\rho R^4 \overline{c}\,\hat{r}_3^3(S)}{2} \tag{S11}$$

$$\Omega_w = \frac{1}{2}\Phi n\left(d\hat{\phi}/d\hat{t}\right) \tag{S12}$$

$$T(\hat{t}) = C\Omega_w^2 \tag{S13}$$

We then add angular velocity due to body motion and write the yaw torques on both wings using the right hand rule to denote the positive direction of yaw:

$$\begin{aligned} T(\hat{t})_{left} &= C\left(\Omega_w - \Omega_b\right)^2 \\ T(\hat{t})_{right} &= -C\left(\Omega_w + \Omega_b\right)^2 \end{aligned} \tag{S14}$$

where $T(\hat{t})_{left}$ is torque on the left wing and Ω_b is the magnitude of instantaneous wing angular velocity due to body angular velocity, given by:

$$\Omega_b = \omega \tag{S15}$$

where ω is yaw angular velocity, with a sign determined by the right hand rule. Note that Eqn. S14 as presented is for downstroke; during upstroke the torque formula for the two wings switches (Fig. 2).

We then arrive at the total torque by summing the torques from the individual:

$$T(\hat{t})_{total} = T(\hat{t})_{left} + T(\hat{t})_{right} = -4C\Omega_w \Omega_b \tag{S16}$$

We then substitute the appropriate kinematic and non-kinematic terms, resulting in:

$$T(\hat{t})_{total} = -4\frac{\rho C_F(\hat{t})\sin(\alpha(\hat{t}))R^4\overline{c}\hat{r}_3^3(S)}{2}\frac{1}{2}\Phi n(d\hat{\phi}/d\hat{t})\omega \tag{S17}$$

This result for a particular instant in non-dimensional time may be converted to a whole-wingbeat mean value by substituting the appropriate whole stroke mean for the production of the time-varying parameters, indicated by the over-bar, and simplifying:

$$T = -\rho\overline{C_F(\hat{t})\sin(\alpha(\hat{t}))(d\hat{\phi}/d\hat{t})}R^4\overline{c}\hat{r}_3^3(S)\Phi n\omega \tag{S18}$$

Converting the total torque to an angular acceleration by dividing by the moment of inertia results in Eqn. 1 from the manuscript:

$$\dot{\omega}_{FCT} = -\omega\frac{\rho R^4\overline{c}\hat{r}_3^3(S)\Phi n\overline{C_F(\hat{t})\sin(\alpha(\hat{t}))(d\hat{\phi}/d\hat{t})}}{I} \tag{S19}$$

This equation is an ordinary differential equation for exponential decay where:

$$\dot{\omega} = -A\omega \tag{S20}$$

From which we can extract a decay half-life:

$$t_{1/2} = \frac{\ln(2)}{A} \tag{S21}$$

and restore *A* to get expressions of half-life in time:

$$t_{1/2}(t) = \frac{\ln(2)I}{\rho R^4\overline{c}\hat{r}_3^3(S)\Phi n\overline{C_F(\hat{t})\sin(\alpha(\hat{t}))(d\hat{\phi}/d\hat{t})}} \tag{S22}$$

and in wingbeats by eliminating wingbeat frequency (*n*) from the denominator:

$$t_{1/2}(N) = \frac{\ln(2)I}{\rho R^4 \overline{c}\, \hat{r}_3^3(S)\Phi\, \overline{C_F(\hat{t})\sin(\alpha(\hat{t}))(d\hat{\phi}/d\hat{t})}}$$

(S23)

In Eqn. S18 we introduced the whole stroke mean for a number of parameters:

$$K = \overline{C_F(\hat{t})\sin(\alpha(\hat{t}))(d\hat{\phi}/d\hat{t})}$$

(S24)

Computation of numerical predictions from this model requires a value for *K*, which we calculated by assuming that wing movement is determined by simple harmonic motion and that wing orientation to incoming flow varied between 0 and 45 degrees during the wing stroke as given by:

$$\alpha(\hat{t}) = \frac{\pi}{4}\left|\tanh\left(2.2\sin(2\pi\hat{\phi})\right)\right|$$

(S25)

We then calculated $C_F(\hat{t})$ using the equation for *Drosophila* force coefficients reported by Dickinson et al. (S*5*) and restated here:

$$C_F(\hat{t}) = \Big(\big(0.225 + 1.58\sin(2.13\alpha(\hat{t}) - 7.20)\big)^2$$
$$+ \big(1.92 - 1.55\cos(2.04\alpha(\hat{t}) - 9.82)\big)^2\Big)^{1/2}$$

(S26)

Following Eqn. S24, we then combined the force coefficient, angle of attack, and non-dimensional angular velocity inputs to give:

$$\overline{C_F(\hat{t})\sin(\alpha(\hat{t}))(d\hat{\phi}/d\hat{t})} \cong 6.0$$

(S27)

This value was used for all species, implicitly assuming that all flying animals have force coefficients similar to those of *Drosophila*, an assumption supported by comparison of force coefficients during constant rotation for a range of animal wings (S*6*). Furthermore, although there may be variation among species in wing force coefficients, the variation is likely to be slight when compared to the range of variation in body size and even wing morphology exhibited among the species examined here.

Limitations and assumptions of the Flapping Counter Torque Model

As described at the beginning of this section, the FCT model presented here is a simplification made possible by the assumption that the coupling terms in Eqn. S6-7 are small relative to the other terms and that roll and pitch velocities are small in comparison to yaw velocity, as shown in the hummingbird recording (Fig. 1) and published fruit fly data (S*1*). We also treat flapping animals as a rigid body, assuming that wing inertial forces play no role in stabilizing flapping flight. Such stabilization is unlikely as net angular momentum from flapping is zero for every half-wingbeat in a symmetrically flapping animal. Our model also includes no forward or indeed any linear velocity terms; the animals are modeled as if they were in hovering flight. This is generally accurate for the data used here, where the largest advance ratio is 0.26 and the mean advance ratio is 0.09, but extension of FCT to forward flight will require incorporation of the effects of forward velocity on the direction and magnitude of aerodynamic torques as well as any adjustments the animals make to wing trajectory, flapping amplitude and other factors. Additionally, the FCT model as constructed here assumes that all flapping animals have identical aerodynamic force coefficients and flap their wings following simple harmonic motion with identical changes in wing orientation and angle of attack. These are unlikely assumptions, but in the absence of detailed information on all species we are left to use a single, fixed set values for all species. Furthermore, we note that the recent recording of a leading edge vortex attached to the wing of a flying bat (S*7*) and measurement of high force coefficients for rotating bird wings (S*6, 8*) suggest that birds and bats may have aerodynamic force coefficients similar to those of insects, at least when flying slowly. More fundamentally, the FCT model is an integrated quasi-steady formulation that derives average flight forces and torques for a complete wingbeat cycle and includes only aerodynamic forces related to wing translation, not those from other sources such as wake capture (S*5*), spanwise wing rotation (S*5*) and clap and fling (S*9*). The quasi-steady nature of the model also suggests that events that happen within a single wingbeat cycle, such as deceleration by a single half life in the hawkmoth, fruit bat and cockatoo examined here, will be less well predicted than events that occur over several wingbeats. Finally, the FCT model assumes symmetric wing motion and force generation during upstroke and downstroke. This is generally accepted for small insects, but does not appear to be the case for hawkmoths (S*10*) and hummingbirds (S*11*) and is certainly not true for larger birds and bats. As long as the mean aerodynamic force over a complete cycle is similar to that predicted by the FCT model and the timescale of events is more than a wingbeat, there is little effect on the model; the hummingbird appears to fall in this category. However, in cases such

as birds and bats where timescales are less than a wingbeat, better predictions could be made if information was available on when in the wingstroke the animal reverted to symmetric motion and began slowing down. Such information is not available so no adjustments were made in this case.

Appendix B: Derivation of deceleration *via* active torque generation

Active torque generation *via* flapping amplitude asymmetry may be modeled by beginning with equation S10, the torque generated by a single wing and introducing a factor γ representing the asymmetry in some portion of the wing properties or kinematics. This is a gross simplification, as asymmetry may take many forms and the type of asymmetry may vary between species. For instance, birds and bats may use asymmetries in wing geometry that cannot be replicated by insects. Nevertheless, we begin with a simple asymmetry and assume that γ represents a temporary reduction in the aerodynamic torque generated by the wing without specifying the underlying mechanism of asymmetry. Inspection of the resulting equations shows that all types of asymmetry that do not vary with time will result in a similar solution, one that predicts linear rather than exponential decay.

$$T(\hat{t}) = \frac{\gamma C_F(\hat{t})\sin(\alpha(\hat{t}))\rho R^4 \bar{c}\hat{r}_3^3(S)\Phi^2 n^2 (d\hat{\phi}/d\hat{t})^2}{8}$$ (S28)

This instantaneous torque may be reduced to a half-stroke mean by introducing mean stroke values for the several time varying constants and combining all non-asymmetric terms in a single constant, *L*:

$$T = \gamma L$$ (S29)

We then assume that the animal generates a net torque over the entire wingbeat cycle by applying the asymmetry during downstroke on the left wing and upstroke on the right wing, giving rise to the following set of per-wing, half-stroke torques:

$$T_{l-up} = -L$$
$$T_{l-down} = \gamma L$$
$$T_{r-up} = \gamma L$$
$$T_{r-down} = -L$$

<div style="text-align:right">(S30)</div>

Note that use of the asymmetry pattern described above, switching the asymmetric wing from left to right between upstroke and downstroke, allows generation of a net torque. Maintaining asymmetry on the same wing during both stroke phases would have no net effect. Summing the quantities in S30 to get total torque due to asymmetry gives:

$$T_{total-up} = T_{l-up} + T_{r-up} = -L + \gamma L = (\gamma - 1)L$$
$$T_{total-down} = T_{l-down} + T_{r-down} = \gamma L - L = (\gamma - 1)L$$
$$T_{mean} = \frac{T_{total-up} + T_{total-down}}{2} = (\gamma - 1)L$$

<div style="text-align:right">(S31)</div>

Expanding L, and dividing by moment of inertia converts this relationship to a mean angular acceleration over a complete wingbeat cycle:

$$\dot{\omega}_a = (\gamma - 1)\frac{\rho R^4 \bar{c} \hat{r}_3^3 (S) \Phi^2 n^2 \overline{C_F \sin(\alpha)(d\hat{\phi}/d\hat{t})^2}}{8I}$$

<div style="text-align:right">(S32)</div>

Finally, an average measure for the non-dimensional wing parameters was required to calculate actual values for deceleration due to wing asymmetry. Following an analysis similar to that in Eqns. S17 – S20, we arrived at:

$$\overline{C_F \sin(\alpha)(d\hat{\phi}/d\hat{t})^2} \cong 31.3$$

<div style="text-align:right">(S33)</div>

Equation S32 expresses the torque that might be expected for a generalized, non-specific aerodynamic force asymmetry. However, all types of morphological or kinematic asymmetry result in a similar overall form: a differential equation for angular acceleration which is independent of angular velocity. Given the absence of experimental data reporting asymmetry, we selected a γ of 0.944, which results in close match to the measured rate of deceleration in *Drosophila* when that rate is measured as the time required to decelerate to one half of peak velocity. A number of different scaling factors could be applied to γ to extend Eqn. 2 to different species. For instance, γ could be varied to increase with wing length, body mass,

or even wingbeat duration[2], preserving $\dot{\omega}_a$ across changes in wingbeat frequency for isometrically scaled animals. However, in the absence of a theory predicting $\dot{\omega}_a$ or γ among species we leave it fixed, exploring the results of scaling by different factors in Appendix D (below).

Finally, we note that the ratio of Equations S32 and S19, describes the balance of active to passive torques at a given rotational velocity and may be used to explore how an animal's capacity to generate accelerative torques changes with the various flapping parameters.

$$\frac{\dot{\omega}_a}{\dot{\omega}_{FCT}} = -(\gamma - 1)\frac{\Phi n \overline{\left(d\hat{\phi}/d\hat{t}\right)}}{8\omega} \tag{S34}$$

Limitations and assumptions of the asymmetric flapping model

This model shares many features of the FCT model presented above and incorporates similar assumptions with attendant limitations. It is also limited, in the practical sense, by the absence of experimental data providing measurement of different types of wing or aerodynamic asymmetry during maneuvers. Thus, we use an asymmetry factor computed to give an accurate result for the fruit fly data and extend it to other species. Therefore the asymmetric flapping predictions are nearly perfect for fruit flies and also quite accurate for other small flying insects, but a poor fit to measurements made on larger flying animals (Table 1).

Appendix C: Yaw turn and morphological data sources

Fruit fly

We used recently published recording of a single yaw (saccade) turn and wingbeat recording for a fruit fly (*Drosophila melanogaster*) (S*1*). Morphological data for the fly were gathered from Fry et al. (S*12*). Fruit fly moment of inertia was estimated using the same cylinder model as Fry et al. (S*1*), tilted to a 50 degree angle to accommodate typical fruit fly flight posture and with the addition of the two wings (see below). The total yaw amplitude of the fly was 90 degrees, mean linear velocity was 0.07 m/s and advance ratio, computed as per (S*13*) was 0.03.

Stalk-eyed fly

We used recently published yaw (saccade) turn and morphological data for male stalk-eyed flies (*Cyrtodiopsis dalmanni*) (S*14*). We selected the yaw velocity profile reported for saccade turns of the 4th quartile of those recorded for incorporation into this analysis; these turns had a mean amplitude of 86 degrees and an average linear velocity of 0.06 m/s. Advance ratio for the stalk-eyed flies was 0.02. Due to their unusual eye position, stalk-eyed flies have a larger moment of inertia than would otherwise be expected for an animal of their size (S*14*).

Bluebottle fly

We used published yaw (saccade) turn and wingbeat data compiled from 121 saccade turns in bluebottle flies (*Calliphora vicina*) (S*15*). Morphological data and some wingbeat kinematic data for this species were gathered from a second source (S*16*). Yaw turn amplitude in these recordings ranged from 60 to 90 degrees; linear velocity was estimated to be 0.5 m/s, the peak of the probability density function reported for all recorded flights. Combined with the wing kinematic data from Table 1, this resulted in an advance ratio of 0.08.

Hawkmoth

Turning dynamics in hawkmoths (*Manduca sexta*) were recorded *via* filming with three calibrated high speed video cameras. Three male hawkmoths were gathered from the laboratory colony maintained at the University of North Carolina at Chapel Hill. The moths were placed in a flight chamber in the presence of a single artificial flower. The chamber was dimly lit in the visible spectrum by a single fluorescent light positioned 6m from the chamber and brightly illuminated in the near-infrared (680 nm), below the moth's visual threshold, by eight infra-red LEDs (Roithner LaserTechnik GmBH, Austria). The moths were filmed as they approached and departed from the flower using three 1000 Hz video cameras (two Phantom v7.1 and one Phantom v5.1; Vision Research, Wayne, NJ). The cameras were calibrated using direct linear transformation (DLT) (S*17, 18*) and three points on the body digitized to allow recovery of rigid body motion. The moths exhibited only slight (less than 5 degrees) flexion between the abdomen and thorax during these turns. A total of six recordings were collected (Fig. S2). Given the variety of yaw turn profiles recorded, rather than averaging or otherwise combining turns we used the data selection parameters applied to the hummingbird recordings (below) and included only the single most rapid and largest amplitude yaw turn in the

interspecific analysis, although this particular event is not as close a match to the model

predictions as some of the other recordings (Fig. S2). In this trial the mean reprojection error for

the body points was 0.82 pixels with a standard deviation of 0.60 pixels. Total yaw amplitude

was 87.8 degrees; the turn was performed at a mean linear velocity of 0.29 m/s for an advance

ratio of 0.07. Morphological data were measured from a population of eight male hawkmoths

from the UNC colony.

Figure S2
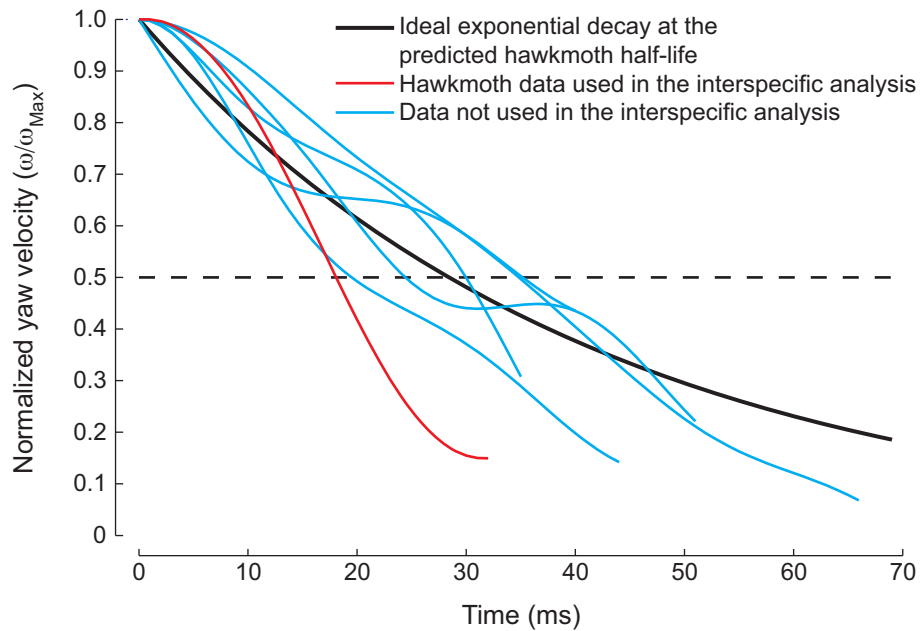
Here we show the six yaw turns recorded from *Manduca sexta* as part
of this analysis, normalized to their maximum angular velocity and
plotted against the exponential decay curve predicted for a hawkmoth
by the FCT model. The turn selected for incorporation in the interspe-
cific analysis (in red) matches the model prediction less well than other
recordings but better satisfies other requirements including high maxi-
mum yaw rate, low advance ratio and absence of provocation or pertur-
bation by the researcher. The average half-life of all six recordings was
28.7 ms, the predicted half-life from the FCT model is 28.4 ms.

Ruby-throated hummingbird

Turning dynamics in hummingbirds were measured by filming them with four

synchronized high-speed video cameras, two of which were coupled with X-ray C-arm imaging

systems, permitting simultaneous light and x-ray recording. Yaw turns occurred incidentally as

the hummingbirds approached or departed from a feeder positioned within the recording

volume. Two female and one male Ruby-throated hummingbirds (*Archilochus colubris*) were captured at Harvard University's Concord Field Station in Bedford, Massachusetts and filmed at 1000 frames per second using two x-ray videograpy systems (Photron 1024pci, Photron USA Inc., San Diego, CA, coupled to an x-ray C-arm system [Model 9400, OEC-Diasonics Inc., Salt Lake City, UT remanufactured by Radiological Imaging Services, Hamburg, PA]) and two visible light video cameras (Phantom v7.1, Vision Research, Wayne, NJ). During the three days of flight recording following capture, the birds were maintained in individual 0.4 x 0.3 x 0.45 m cages with food and water provided *ad libitum*. Prior to recording, the birds were each implanted with three subdermal x-ray opaque markers which provided the three fixed body points required to compute yaw, pitch and roll orientation. The x-ray and light video cameras were calibrated using DLT with pre-processing of the x-ray images to remove all optical distortion introduced by the multiple lenses and image intensifier (S*19*). The single most rapid yaw and largest amplitude turn was selected for analysis, in this trial the mean reprojection error for the three points was 1.34 pixels with a standard deviation of 0.47 pixels. Total yaw amplitude during the turn was 149.6 degrees, the mean forward velocity during the turn was 0.15 m/s, resulting an in advance ratio of 0.01. Hummingbird data were provided by Dr. Andrew A. Biewener of Harvard University; the experiments were performed in accordance with Harvard University Institutional Animal Care and Use guidelines. Morphological data were measured from a group of three hummingbirds, two females and one male. The turn analyzed was performed by a female.

Lesser Short-nosed Fruit bat

Turning dynamics in the Lesser Short-nosed Fruit bat (*Cynopterus brachyotis*) were measured by filming the bat with three synchronized high-speed video cameras (Photron 1024pci, Photron USA Inc., San Diego, CA). The cameras were calibrated using DLT. Body orientation was measured using three fixed points on the body as the bat flew up and out of an enclosed space, an open box of dimensions 0.6 x 0.6 x 0.6 m in width x length x height. Only a single recording of bat turning was available for analysis; mean reprojection error for the body points used to determine orientation was 1.05 pixels with a standard deviation of 0.44 pixels. Total yaw amplitude during the recorded turn was 165 degrees and the bat's mean linear velocity was 1.5 m/s, resulting in an advance ratio of 0.18. The bat was part of a colony maintained indefinitely at Brown University; animal care procedures and experimental recordings were in accordance with Brown University Institutional Animal Care and Use

guidelines. The bat data were provided by Drs. Sharon Swartz and Kenneth Breuer of Brown University. Morphological data were measured from a group of two bats.

Rose-breasted cockatoo

Previously unpublished data from the cockatoo (*Eolophus roseicapillus*) turning experiments described in (S*20*) were analyzed to provide the yaw turn data for this species. The experimental, animal care, and analysis protocol were those previously described in (S*20*), except that the cockatoos were forced to reverse course in mid-flight, executing a 180 degree turn rather than the 90 degree turn they were trained to perform. Morphological data were measured from a group of six cockatoos. In the turn analyzed for this manuscript, the total yaw rotation was 186 degrees performed at an average linear velocity of 2.2 m/s, resulting in an advance ratio of 0.26.

Analysis of measurement error

Measurements of angular velocity in freely behaving animals are potentially subject to substantial error. Furthermore, due to the diversity of sources and recording methods used to acquire the data incorporated in this manuscript, measurement error likely varies between species. Finally, kinematic data and especially differentiated kinematic data are typically subjected to a low pass filter of some type and this filtering might alter some of the parameters reported here such as peak yaw velocity and duration of the first half life. Exact measurement of peak velocities is not important to our analysis, but measurement of half life duration is critical. Any low pass filter leads to a slight increase in the measured half life of an ideal exponential decay curve, but the error does not exceed 10% of the actual value as long as the low-pass filter cutoff frequency is greater than one divided by the half life in seconds. This was not the case for any of the data examined here (see below). Nevertheless, any amount of low pass filtering will change the shape of an exponential decay curve, making it more sinusoidal at the beginning of decay and preventing accurate measurement of half life from the initial decay trajectory. This effect is apparent to a greater or lesser degree in all the recordings used here, where the trajectory match to exponential decay is initially poor (Fig. 2D) but improves thereafter. Of the data sources noted above, the fruit fly data were not accompanied by any information on possible measurement error, but Fourier analysis of the published recordings suggests that a low-pass filter with a cutoff frequency of approximately 200 Hz. This cut-off

frequency is greater than the predicted half-life frequency of 109 Hz and should not prevent accurate measurement of the duration of the first half life. The stalk-eyed fly data were filtered at 60 Hz, again well above the expected half life frequency, as were the bluebottle fly data which were filtered at 250 Hz. The resolution of the recordings systems used with the hawkmoth, hummingbird, fruit bat and cockatoo data result in a measurement uncertainty of approximately 1.0, 0.5, 2.0 and 2.0 degrees, respectively and the recordings were filtered using a smoothing spline with the above noted error tolerance. This, combined with the different recording rates, resulted in effective cutoff frequencies of approximately 64, 110, 48 and 44 Hz, all of which are greater than the predicted half-life frequencies of 35, 45, 35 and 33 Hz. Thus, although there may be a systematic trend toward measurement of greater than actual half-lives due to low-pass filtering, it should be less than 10% in the worst case and less than 5% in most cases. Some deviation from exponential decay is expected at the start of all deceleration recordings; deviation will take the form of a shallower initial slope.

Calculation of moment of inertia

For the above species, moment of inertia about the global yaw axis was estimated by modeling the animal as a cylinder with attached wings, with the further assumption that each species pitched up at an angle of 50 degrees during these hovering or low speed maneuvers. Thus, for the cylinder body we first computed I_{zz} and I_{xx}, moments about the body frame yaw and roll axes as:

$$I_{zz} = mass \frac{1}{12}\left(height^2 + 3radius^2\right) \tag{S35}$$

$$I_{xx} = mass\left(\frac{1}{2}radius^2\right) \tag{S36}$$

We then applied the 50 degree pitch angle to the cylinder to calculate I_{zzt}, the moment of inertia for the body about the inertial yaw axis, which is coincident with the stroke plane yaw axis in this analysis (Fig. S1):

$$I_{zzt} = \cos(pitch)^2 I_{zz} + \sin(pitch)^2 I_{xx} \tag{S37}$$

The wings of each species were modeled as a rectangular plate rotated about the center of mass of the animal; total wing mass was assumed to be 1% of body mass for *Calliphora* and smaller animals (S*16*) and 10% of body mass for the fruit bat. Actual wing moments of inertia were available for the hawk moth, hummingbird and cockatoo.

$$I_{wings} = mass_{wings} \left(\frac{1}{3} R^2 + \frac{1}{12} \bar{c}^2 \right) \tag{S38}$$

The wings stroke plane was assumed to be in the global horizontal regardless of body tilt. Thus, the final estimated moment of inertia, I'_{zz} was calculated as the sum of I_{zzt}, the moment of inertia of the body about the stroke plane frame yaw axis, and I_{wings}. In cases where intermediate values in our moment of inertia scheme such as I_{zz} or I_{xx} were available from direct measurements, these were substituted for the estimated values.

**Appendix D: Scaling flapping asymmetry (γ)**

As described above in Appendix B, we used a γ of 0.944 in all species for predicting the dynamics of deceleration by flapping asymmetry. This value for γ was arrived at by measuring the deceleration dynamics of the fruit fly and solving for an appropriate γ to match the measured dynamics. Clearly, as indicated in Eqn. 4, this results in a prediction of deteriorating maneuvering performance for animals with a lower wingbeat frequency, an attribute typical of larger animals. In the absence of an accepted theory for varying asymmetry with size and the assumption that maneuvering performance does decrease with size, we did not apply a scaling factor to γ. However, the data collected for this paper might reveal a scaling trend for γ if such a trend exists. With this goal, we recalculated our predictions for active deceleration after applying a variety of scaling rules to γ: scaling based on moment of inertia, body mass, characteristic length, and the inverse of frequency[2] (Fig. S2). None of these scaling attempts matched the observed trends and none of them was a better predictor of the observed dynamics than the FCT predictors or even the original, unscaled γ.

Scaling was applied as:

$$\gamma' = (\gamma - 1)SF + 1 \qquad\qquad\qquad\qquad (S39)$$

where *SF* is the scale factor between *Drosophila* and the animal in question along the dimension of interest. For example, if the animal in question has three times the body mass of *Drosophila*, scaling γ by body mass would result in a γ' of 0.832 for the animal in question.

Figure S3
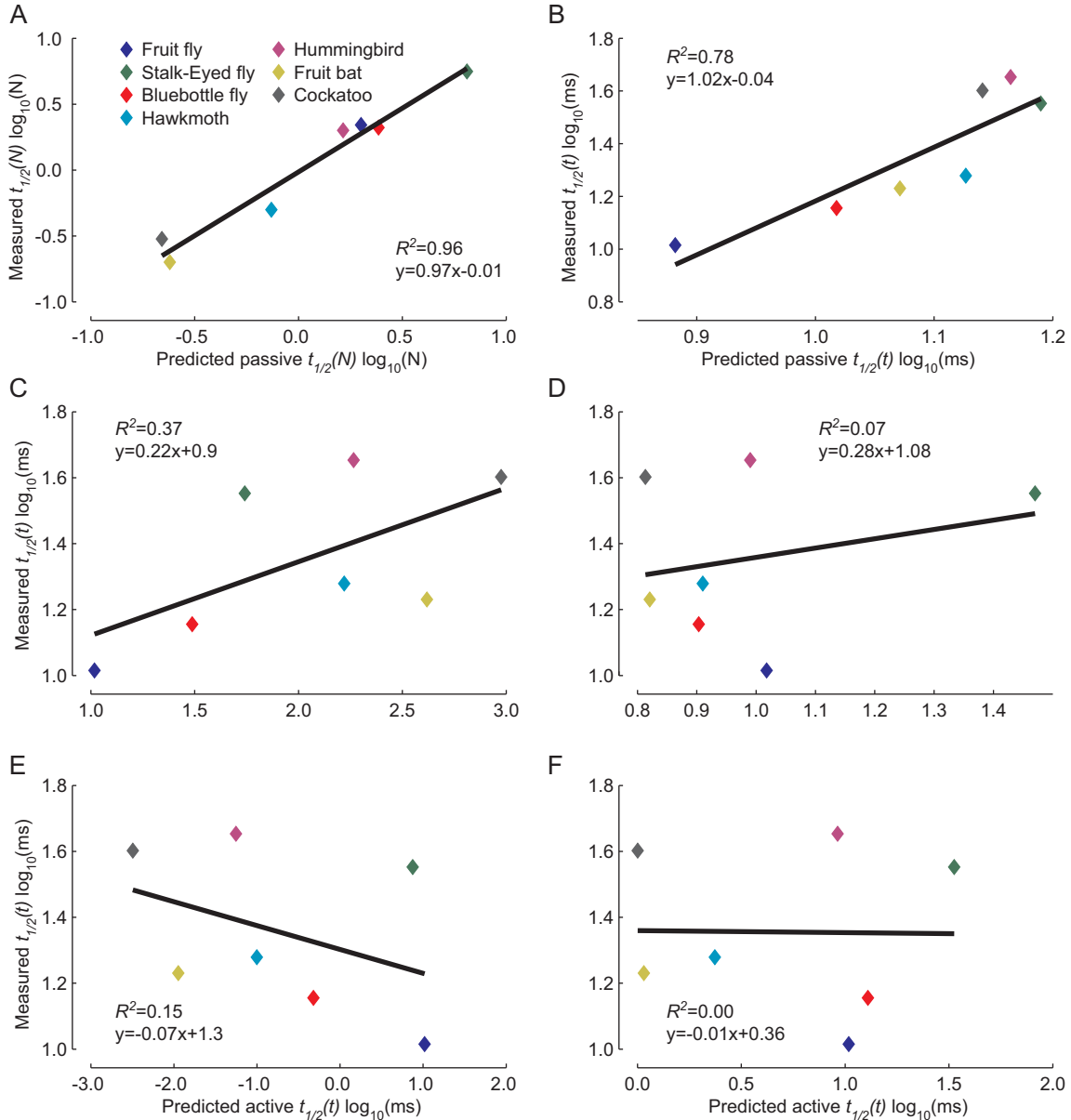
Here we show a scatterplot and least-squares regression results for log-transformed data of all predictions and measurements, including predictions using a scaled γ. In this context, an accurate predictor will have an R^2 near 1.0, a regression slope near 1.0 and a regression intercept near 0.0 as exemplified by the results in (A), the FCT prediction of deceleration half-life in wingbeats and (B) the FCT prediction of deceleration half-life in milliseconds, (C) deceleration time with γ of 0.944 for all species. Neither the R^2 nor regression slope indicates a good fit. (D) deceleration time with γ scaled by wing length. (E) deceleration time with γ scaled by body mass. (F) deceleration time with γ scaled by the square of wingbeat duration, a factor that results in similar deceleration rates in all species in the active deceleration model.

Table S1: Here we compute the scaling of body and wing dimensions relative to the fruit fly for all other animals examined here. All values were reduced to a scaling of a characteristic length. For example, the characteristic length scale of an animal with a body mass 10 times greater than that of a fruit fly is $(10/1)^{(1/3)}$.

Species	Morphology				Averages		
	mass	I'_{zz}	*R*	$\bar{c}$	*Average body*	*Average wing*	$\dfrac{Wing}{Body}$
Fruit fly (*Drosophila melanogaster*)	1	1	1	1	1	1	1
Stalk-eyed fly (*Cyrtodiopsis dalmanni*)	1.9	2.3	1.9	1.2	2.1	1.6	0.76
Bluebottle fly (*Calliphora vicina*)	4.0	4.0	3.8	3.9	4.0	3.9	0.98
Hawkmoth (*Manduca sexta*)	11.9	15.5	20.4	23.3	13.7	21.9	1.60
Hummingbird (*Archilochus colubris*)	14.9	16.7	18.8	14.8	15.8	16.8	1.06
Fruit bat (*Cynopterus brachyotis*)	33.2	43.3	62.7	103	38.3	82.9	2.16
Cockatoo (*Eolophus roseicapillus*)	66.8	86.1	145.2	147.5	76.5	146.4	1.91

Supplementary References:

S1.   S. N. Fry, R. Sayaman, M. H. Dickinson, *Science* **300**, 495 (2003).
S2.   M. F. M. Osborne, *J. Exp. Biol.* **28**, 221 (1951).
S3.   C. P. Ellington, *Phil. Trans. R. Soc. Lond. B* **305**, 79 (1984).
S4.   S. P. Sane, M. H. Dickinson, *J. Exp. Biol.* **204**, 2607 (2001).
S5.   M. H. Dickinson, F.-O. Lehmann, S. P. Sane, *Science* **284**, 1881 (1999).
S6.   J. R. Usherwood, C. P. Ellington, *J. Exp. Biol.* **205**, 1565 (2002).
S7.   F. T. Muijres *et al.*, *Science* **319**, 1250 (2008).
S8.   J. Usherwood, *Exp. Fluids* 10.1007/s00348-008-0596-z.
S9.   T. Weis-Fogh, *J. Exp. Biol.* **59**, 169 (1973).
S10.   A. P. Willmott, C. P. Ellington, *J. Exp. Biol.* **200**, 2723 (1997).
S11.   D. R. Warrick, B. W. Tobalske, D. R. Powers, *Nature* **435**, 1094 (2005).
S12.   S. N. Fry, R. Sayaman, M. H. Dickinson, *J. Exp. Biol.* **208**, 2303 (2005).
S13.   C. P. Ellington, *Phil. Trans. R. Soc. Lond. B* **305**, 41 (1984).
S14.   G. Ribak, J. Swallow, *J. Comp. Physiol. A* **193**, 1065 (2007).
S15.   C. Schilstra, J. H. van Hateren, *J. Exp. Biol.* **202**, 1481 (1999).
S16.   A. R. Ennos, *J. Exp. Biol.* **142**, 49 (1989).
S17.   Y. I. Abdel-Aziz, H. M. Karara, paper presented at the Proceedings of the Symposium on Close-Range Photogrammetry, University of Illinois at Urbana-Champaign 1971.
S18.   R. Hartley, A. Zisserman, *Multiple view geometry in computer vision* (Cambridge University Press, New York, New York, USA, ed. 2nd, 2003).
S19.   E. L. Brainerd, S. M. Gatesy, D. B. Baier, T. L. Hedrick, *J. Morphol.* **268**, 1053 (2007).
S20.   T. L. Hedrick, A. A. Biewener, *J. Exp. Biol.* **210**, 1897 (2007).